Scilight

Electromagnetic Wave Science and Technology
https://www.sciltp.com/journals/ewst

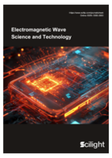

Article

A Meta-Aramid-Based Composite with Strong Abrasion-Resistance Enabled by Sandwich and Brick-Mortar Architectures for Electromagnetic Shielding and Strain Sensing

Jiafei Wang [1,2], Rongjun Qu [1,*], Xinyu Li [1], Fang Ma [3], Ying Zhang [1], Jiaru Li [1], Liangfan Gong [1], Ying Wang [1], Changmei Sun [1,*], Xiquan Song [2,*], Qianli Ma [2], Xue Geng [2], Xiangyu Kong [2] and Ran An [2]

[1] School of Chemistry and Chemical Engineering, Ludong University, Yantai 264025, China
[2] Yantai Tayho Advanced Materials Co., Ltd., Yantai 264006, China
[3] College of Chemical Engineering and Technology, Yantai Nanshan University, Yantai 265713, China
* Correspondence: rongjunqu@sohu.com (R.Q.); sunchangmei0535@126.com (C.S.); ytaramid@163.com (X.S.)

How To Cite: Wang, J.; Qu, R.; Li, X.; et al. A Meta-Aramid-Based Composite with Strong Abrasion-Resistance Enabled by Sandwich and Brick-Mortar Architectures for Electromagnetic Shielding and Strain Sensing. *Electromagnetic Wave Science and Technology* **2026**, *1*(1), 1.

Received: 25 December 2025
Revised: 30 January 2026
Accepted: 25 February 2026
Published: 12 March 2026

Abstract: The proliferation of electronic devices has intensified concerns on electromagnetic radiation pollution. Metal-coated polymer fabrics, particularly those possessing electromagnetic shielding and sensing capabilities, encounter significant challenges arising from metal layer degradation during use. Herein, a super-abrasion-resistant composite, PMIA/HPAMAM-EGDE/Ag@TPU (PHEAT), was fabricated using meta-aramid (PMIA) fabric as the substrate, the hyperbranched polyamidoamine (HPAMAM) crosslinked with ethylene glycol diglycidyl ether (EGDE) as the surface activator, electroless plated silver (Ag) as the conductive layer, and thermoplastic polyurethane (TPU) film as the protective coating. The obtained PHEAT features an internal brick (PHEA fiber)-mortar (TPU) microstructure and an external TPU-PHEA-TPU sandwich macrostructure. This robust geometric architecture synergistically improves the mechanical strength of PHEA while maintaining the inherent flexibility, lightness, and thinness of PMIA fabric. Remarkably, after 1000 abrasion cycles using 600-grit sandpaper, PHEAT-0.05 (initial total shielding effectiveness, SE_T = 101.57 dB) and PHEAT-0.1 (SE_T = 73.94 dB) still retained the high SE_T values of 52.95 dB and 59.63 dB, respectively, corresponding to 99.999493% and 99.99989% shielding efficiency of incident electromagnetic wave. Furthermore, PHEAT exhibits reliable and repeatable relative resistance change signals during cyclic bending strain and human joint movements, demonstrating significant potential for flexible sensing applications. These findings pave a new way for the development of advanced flexible electronics with integrated functionalities.

Keywords: meta-aramid fabric; sandwich and brick-mortar architectures; abrasion-resistant composite; electromagnetic interference shielding; flexible strain sensing

1. Introduction

The widespread use of X-band electromagnetic wave (EMW) (ranging from 8.2 to 12.4 GHz) in advanced fields, such as radar systems, telecommunications, and space technologies, necessitates effective mitigation of electromagnetic pollution to protect both human health and electronic equipment [1–3]. Thin, light, wide and strong conductive polymer fabric-based composites (CPFCs) capable of shielding over 99% of EMW (total shielding effectiveness, $SE_T > 20$ dB) have been engineered to address electromagnetic interference (EMI). These materials inherit the pliability, lightness, and thinness of the polymer fabric substrates [4,5]. Nonetheless, achieving a balance between high EMI shielding performance and sustained mechanical integrity and abrasion resistance remains a formidable challenge for CPFCs in practical applications.

Meta-aramid (PMIA) stands out amongst polymer fabrics due to its exceptional mechanical strength, dimensional stability, thermal resistance, flame retardancy, chemical resilience, radiation tolerance, and inherent abrasion resistance, making it well suitable for demanding applications in military, defense, firefighting, aerospace, high-tech equipment, new energy, and advanced industries [6]. Conductive PMIA fabric is typically prepared by depositing active conducting materials, such as one-dimensional and two-dimensional metal particles/wires, conductive carbon materials, transition metal carbide and/or nitride, onto the non-conductive PMIA surface [7] by spray coating [8], screen printing [9], vacuum filtration [10], electrodeposition [11], or electroless plating [12]. Electroless silver (Ag) plating is widely preferred for its minimal equipment requirements, operational simplicity, high efficiency, capability to deposit continuous and highly conductive layers, and low impact on the intrinsic properties of PMIA [13]. Moreover, the interconnected network of cross-arranged fibers of Ag-plated PMIA can enhance EMI shielding efficiency by offering multiple internal reflections of EMW. However, in practical applications, mechanical washing, bending, peeling, and abrasion can cause the detachment of surface Ag layer, leading to notable reductions in SE_T. To address this issue, bridging materials, such as polydopamine, poly(3,4-ethylene dioxythiophene):poly(styrenesulfonate), and hyperbranched polyamidoamine (HPAMAM) that can firmly bond the Ag-to-PMIA, have been introduced. The resulting CPFCs can achieve SE_T over 50 dB and resist bending, winding, and moderate abrasion [6,14,15]. Building upon the construction of an interfacial adhesion layer between Ag and PMIA, further coating the outer Ag surface with a fluorine-containing agent or polydimethylsiloxane (PDMS) can improve the resistance to washing and tape peeling; however, the protection against severe abrasion, such as coarse sandpaper abrasion, remains insufficient [4,15].

Thermoplastic polyurethane (TPU), known for its high strength, elasticity, flexibility, outstanding abrasion resistance, shock absorption, and skid resistance, are extensively used in elastic fibers, tires, insulators, etc. [16]. Inspired by the efficacy of TPU in protecting materials against stainless steel ball friction [17], grinding wheel abrasion [18], as well as sand impact, scalpel scratch and sandpaper scrape [19,20], a TPU layer was integrated onto the HPAMAM-modified Ag-plated PMIA fabric via hot-pressing to form a PMIA/HPAMAM-EGDE/Ag@TPU (PHEAT) composite (PHEA denotes PMIA/HPAMAM-EGDE/Ag and EGDE is ethylene glycol diglycidyl ether). During the hot-pressing, softened TPU fills the inter-fiber voids within the PHEA fabric, creating an internal brick (PHEA fiber)-mortar (TPU) microstructure and an external TPU-PHEA-TPU sandwich macrostructure which ensure strong interfacial bonding. This design observably enhances the mechanical robustness of PHEA while preserving its pliability, lightness, and thinness. Notably, PHEAT-0.05 ($SE_T = 101.57$ dB) and PHEAT-0.1 ($SE_T = 73.94$ dB), incorporating ultrathin TPU layers of 0.05 and 0.1 mm respectively, retained SE_T values of 52.95 dB and 59.63 dB even after 1000 abrasion cycles using 600-grit sandpaper, approaching the standard for military application (60 dB) [21]. However, after only 100 abrasion cycles with 1500-grit sandpaper, the SE_T of PHEA (107.66 dB) and PHEAP (PMIA/HPAMAM-EGDE/Ag/PDMS, 103.79 dB) decreased significantly to 34.12 dB and 46.37 dB, respectively, underscoring the critical protective role of TPU over PDMS for PHEA under harsh physical environments. In addition, the flexible PHEAT exhibited consistent and reversible relative resistance change under cyclic strain and human joint motions, highlighting its potential in sensing applications. Our study pioneers a new pathway for developing abrasion-resistant CPFCs with strong of EMI shielding and strain sensing capabilities.

2. Experimental Procedures

2.1. Materials

PMIA fabric and HPAMAM were purchased from Tayho Advanced Materials Co., Ltd., Yantai, China and CY Dendrimer Technology Co., Ltd., Weihai, China, respecitvely. EGDE, anhydrous ethanol, ammonium hydroxide (NH_4OH, 25–28%), silver nitrate ($AgNO_3$), potassium hydroxide (KOH), polyvinylpyrrolidone (PVP, K30), anhydrous glucose, polyethylene glycol 2000 (PEG), and *n*-heptane were provided by Sinopharm Chemical Reagent Co., Ltd., Shanghai, China. PDMS (SYLGARD 184 Silicone Elastomer Base) and curing agent were supplied by Dow Silicones corporation, Midland, TX, USA. Commercially available TPU film was purchased from a local market in Dongguan, China. Ultrapure water ($0.05\ \mu S \cdot cm^{-1}$) was produced in-house using an ultrapure water system (UPH-I-40L, Super Pure Technology Co., Ltd., Chengdu, China). All chemicals were of analytical grade and used without any further purification.

2.2. Assembly of PMIA/HPAMAM-EGDE/Ag

The inherent chemical inertness and low surface energy of PMIA result in a weak chelation ability toward Ag. HPAMAM, a low-cost modifier rich in amino/carbonyl groups and nanoscale cavities, can enable extensive adsorption and chelation of Ag. EMI shielding PMIA fabric was first prepared via HPAMAM modification combined with electroless Ag plating as described in our previous study [15]. Briefly, the PMIA fabric (50 mm × 40 mm) was sequentially ultrasonically cleaned with anhydrous ethanol and ultrapure water for 30 min each (30 °C, 40 kHz, 252 W) to remove oil stains and other impurities on surface and dried in a vacuum oven at 60 °C to remove the ethanol and water residues for the subsequent loading of HPAMAM-EGDE. The HPAMAM-EGDE modification solution was prepared by adding 1.0 g HPAMAM and 0.586 mL EGDE into 200 mL ultrapure water, followed by the reaction at 70 °C for 60 min under magnetic stirring, and then divided into two equal portions. A portion was dried at 60 °C to obtain HPAMAM-EGDE gel for chemical structure characterization. The cleaned PMIA fabric was immersed in the another portion of HPAMAM-EGDE solution for over 60 min, and solidified in the vacuum oven at 60 °C to obtain PMIA/HPAMAM-EGDE (denoted as PHE) modified fabric.

Under vigorous stirring, 2.5 mL NH_4OH was added dropwise into a $AgNO_3$ solution in ultrapure water ($25\ g{\cdot}L^{-1}$, 86.6 mL). The pH of the solution was adjusted to approximately 11.0 using about 10.5 mL KOH ($6\ g{\cdot}L^{-1}$). Following the addition of 0.4 mL NH_4OH, 0.5 g PVP ($5\ g{\cdot}L^{-1}$) was added to obtain a stable Ag ammonia solution. Subsequently, 3 g glucose, 4 mL anhydrous ethanol and 7.5 mg PEG were added into 100 mL ultrapure water to form a glucose reducing solution with the concentration of $30\ g{\cdot}L^{-1}$. Following a standard procedure, the PHE fabric was soaked in the Ag ammonia solution and subjected to ultrasonic treatment for 30 min to allow adequate chelating adsorption reaction for a high-quality Ag layer on the fabric surface. Subsequently, the glucose reducing solution was added at the rate of $1\ drop{\cdot}s^{-1}$, and the reduction reaction was continued for 60 min. After the adsorption-reduction of Ag on the surface of PHE was completed, the reaction system was allowed to stand still until the solution was clarified. The fabric was then taken out, thoroughly rinsed with pure water to remove the unfixed Ag granules, and vacuum dried at 60 °C to obtain PMIA/HPAMAM-EGDE/Ag (PHEA). PHEAP composite was then fabricated following the procedure outlined in our previous study [15]. A homogeneous PDMS solution was formulated by stirring PDMS (1 g) and the curing agent (0.1 g) in *n*-heptane (98.9 g) for 10 min. PHEA was immersed in the PDMS solution for 40 min and dried under vacuum at 60 °C to afford PHEAP.

2.3. Construction of PMIA/HPAMAM-EGDE/Ag@TPU

In light of the significant reduction in SE_T caused by the poor abrasion resistance of the Ag layer on the fabric surface, a layer of TPU film was applied to the surface of PHEA by hot-pressing to form a fully bonded interface. Specifically, two TPU films with the sizes of 50 mm × 40 mm were attached onto the upper and lower surfaces of PHEA and hot-pressed at 150 °C for 2 min. The composite was cooled in another hot press at room temperature for 30 s to obtain the abrasion-resistant PMIA/HPAMAM-EGDE/Ag@TPU, denoted as PHEAT-X (or PHEAT if the thickness not specified) where X (0.05, 0.1, 0.15, 0.2, 0.25, or 0.3 mm) is the thickness of the TPU prior to hot-pressing.

2.4. Characterization

The chemical structures of HPAMAM, HPAMAM-EGDE, PMIA, PHE, PHEA, TPU, and PHEAT were characterized by Fourier transform infrared spectroscopy (FTIR) using a FTIR spectrometer (Nicolet iS50, Thermo Fisher Scientific, Waltham, MA, USA). The surface morphologies and elemental compositions and distributions of PMIA, PHE, PHEA, PHEAP, and PHEAT were imaged by scanning electron microscopy (SEM) using a GeminiSEM300 electron microscope equipped with an energy dispersive spectroscope (ZEISS, Oberkochen, Germany). The mechanical attributes of PMIA, PHEA, and PHEAT (10 mm in width) were measured using an electronic universal testing machine (5967, Instron, Norwood, MA, USA) at a tensile rate of $100\ mm{\cdot}min^{-1}$ and gauge length of 20 mm. The crystal structures of PHEA and PHEAT were examined by X-ray diffractometry (XRD) using an Ultima IV diffractometer (Rigaku, Shojima, Japan). The electrical conductivity and sheet resistance of PHEA and PHEAT were measured using a multifunctional digital four-probe tester (ST-2258C, Jingge Electronic Co., Ltd., Suzhou, China). The abrasion resistances of PHEA, PHEAP, and PHEAT were investigated using a fastness tester (YB571BC, Darong Textile Instrument Co., Ltd., Wenzhou, China). The strain sensing performance of PHEAT was monitored using a data acquisition multimeter system (DAQ6510, Keithley, Cleveland, OH, USA) integrated with a hand-held automatic flexible bending tester (PR-BDM3-100P, Purui Materials Technology Co., Ltd., Shenzhen, China).

The EMI shielding performances of PHEA, PHEAP, and PHEAT (22.86 mm × 10.16 mm) in the X-band frequencies ranging from 8.2 to 12.4 GHz were evaluated by the waveguide method using a vector network analyzer (ZNB20, Rohed *&* Schwarz, Munich, Germany). The EMW scattering parameters, S_{11} and S_{21}, were read from the vector network analyzer. The reflection coefficient (*R*), transmission coefficient (*T*), absorption coefficient (*A*), surface reflection effectiveness (SE_R), absorption effectiveness (SE_A), total effectiveness (SE_T), and shielding efficiency in percentage ($SE_{\%}$) of the material are derived by the equations below [22]:

$$R = |S_{11}|^2, \quad T = |S_{21}|^2, \quad A = 1 - R - T \tag{1}$$

$$SE_R = -10\log(1-R), \quad SE_A = -10\log\left(T/(1-R)\right) \tag{2}$$

$$SE_T = SE_R + SE_A, \quad SE_{\%} = \left(1 - 10^{-SE_T/10}\right)\times 100 \tag{3}$$

The actual far-field EMW dissipation mechanism of PHEAT in real situations was illustrated by radar cross-section (*RCS*) simulation using the computer simulation technology (CST) microwave studio software. The thicknesses of the perfect electric conductor (PEC), PHEAT-0.05 and PHEAT-0.1 were set at 1.0, 0.5 and 0.52 mm respectively, and the model side was set to 180 mm to accelerate the simulation. The model was positioned in the *x-o-y* plane, oriented along the positive *z*-axis. A linearly polarized plane EMW, propagating along the *z*-axis the positive to negative, was introduced as the excitation source. The electric filed was aligned parallel to the *x*-axis, while the magnetic field was perpendicular to it. The representative EMW frequency of 10 GHz within the X-band was selected as the monitoring frequency to compare the EMW reflection competence of PHEAT with that of PEC. The *RCS* value is defined as [23]:

$$RSC(dB\cdot m^2) = 10\log((4\pi S/\lambda^2)\left|E_s / E_i\right|)^2 \tag{4}$$

where S is the area of the simulated model, λ is the incident EMW wavelength, E_s and E_i are the electric field intensities of scattered and incident EMW, respectively.

3. Results and Discussion

3.1. Fabrication and Characterization of PHEAT

Figure 1a is the schematic illustration of the fabrication process for the sandwich-structured PHEAT. HPAMAM is first crosslinked with EGDE via a ring-opening addition between the epoxy and amine groups to yield HPAMAM-EGDE. The FTIR spectrum in Figure 1b confirms the successful synthesis with a discernibly broadened peak at 3300 cm^{-1} and the appearance of new peaks at 1085 and 935 cm^{-1} [24]. PMIA fabric is subsequently immersed in HPAMAM-EGDE, during which the hydrogen bonding occurs between the amino groups of HPAMAM and the amide C=O/N–H groups of PMIA. The interaction creates a well-adhered surface layer that efficiently smooths the surface defects (Figure 2a,b) and enhances the interfacial adhesion between the subsequent Ag and PMIA substrate. The FTIR peaks of HPAMAM-EGDE in PHE are not distinctly observable, possibly due to its relatively low loading content and the resulting lack of pronounced improvement in functional groups [3]. This suggests that the dip-coating treatment exerts only a marginal influence on the intrinsic properties of PMIA fabric, such as mechanical strength, thermal stability, and crystallization [15]. During the electroless plating, the N/O atoms and the nanoscale cavities in the modified PHE chelate Ag^+ ions, which are subsequently reduced in situ to form a dense and highly conductive Ag layer (Figure 2c). This is evidenced by all the suppressed characteristic peaks in the FTIR spectrum of PHEA [9]. The PHEA fabric exhibits closely packed network of crisscrossed fibers and small voids between them, which are conducive to multiple reflections and scattering of EMW. The detailed reaction mechanisms including HPAMAM crosslinking, PMIA surface modification and electroless Ag plating can be found in our previous studies [15,24].

Pioneering work [15] demonstrates that Ag-plated PMIA fabric can maintain high SE_T even after 2000 bend-stretch cycles, 200 wind-release cycles, and 200 weight abrasion cycles. The incorporation of a PDMS layer further improve the resistance to washing (5 cycles) and tape peeling (5 cycles), but it is insufficient under severe sandpaper abrasion, as discussed in the abrasion resistance performance section below. To address this limitation, the highly abrasion-resistant TPU is integrated onto PHEA by hot-pressing. The resultant sandwich-structured PHEAT consists of TPU films as the top and bottom layers and PHEA fabric as the middle layer which are strongly bonded at the interfaces by hot-pressing at 150 °C (Figure 1a). As shown in Figure 1b, the characteristic FTIR peaks of PHEAT highly resemble those of TPU, definitively underlining the successful integration TPU in PHEAT [18,20]. PHEAT maintains the lightness and flexibility (digital photographs in the inset in Figure 1c), as well as the mechanical strength of the fabric well. Notably, the Ag plating process reduces the tensile strength of PMIA from 48.4 to 40.4 MPa, while TPU assembly increases the strength of PHEA by 23.3% to 49.8 MPa. XRD analysis reveals an increasing intensity of the broad amorphous TPU peak centered at 20° with the increasing of TPU thickness (Figure 1d) [18]. Meanwhile, the hot-pressing process causes no significant effect on the high crystallinity of the Ag layer, which exhibits the characteristic peaks at 38.1° (111), 44.3° (200), 64.5° (220), 77.4° (311), and 81.6° (222) [25]. This indicates that the TPU forms a protective surface coating without altering the internal crystalline structure of PHEA, thereby maintaining its EMI shielding capacity. The elemental mapping analysis of C, N, O, and Ag (Figures 2f and S1d–g) suggests that thin TPU layers (e.g., PHEAT-0.05 and PHEAT-0.1) preferentially fill fabric voids, leaving some regions exposed with some Ag particles visibly present. With the increasing thickness, TPU progressively covers these exposed areas. SEM analysis confirms a compact Ag coating on individual fibers (Figure 2d), the efficient infiltration of TPU into the inner surfaces of the fabric and uniform coverage of TPU on the outer surface (Figure 2e), which form an internal tightly-linked brick (PHEA fiber)-mortar (TPU) microstructure [26] and an external tightly-bonded TPU-PHEA-TPU sandwich configuration [21]. As shown in Figure S2a, C, N, O, and Ag are uniformly dispersed across the cross-section of PHEA. Figure S2b indicates that Ag is distributed in the middle of PHEAT, while C, N, and O are evenly distributed throughout its entire cross-section. The structurally complementary macro-micro sandwich and brick-mortar geometric design is expected to protect the plentiful Ag network from damages caused by abrasion or bending, thereby endowing the PHEAT CPFCs with integrated abrasion-resistant EMI shielding and reliable strain sensing capabilities. Another noteworthy finding is that the thickness of PHEAT decreases first and then increases relative to PHEA as the TPU thickness increases, further providing a clear evidence of the progressive filling of surface voids in the PHEA fabric and the formation of fully bonded PHEA-TPU interface under hot-pressing (Figure S1h–l).

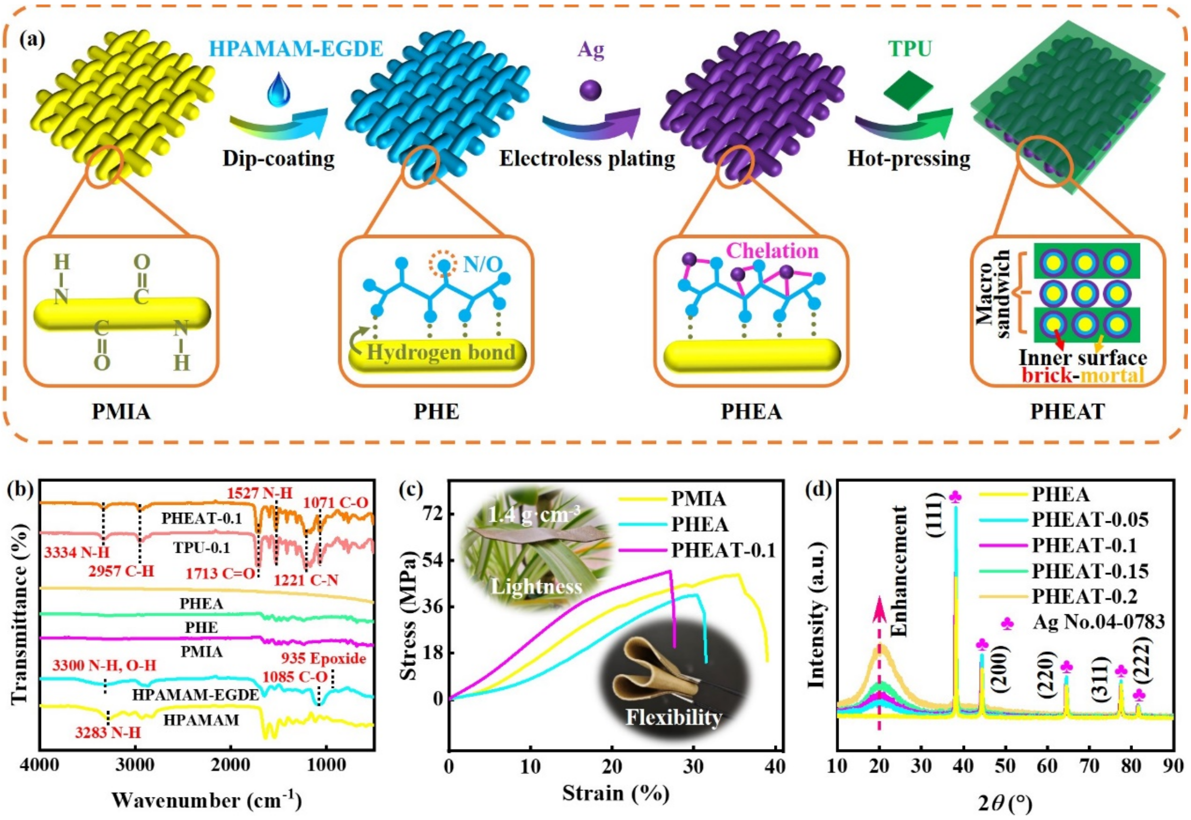

Figure 1. Construction and characterization of PHEAT. (**a**) Schematic diagram illustrating the fabrication process of PHEAT, involving the surface modification of PMIA with HPAMAM-EGDE, electroless Ag plating, and hot-pressing with TPU; (**b**) FTIR spectra of different composites; (**c**) Tensile stress-strain curves with the insets demonstrating the lightness and flexibility of PHEAT-0.1; (**d**) XRD patterns of PHEAT-X.

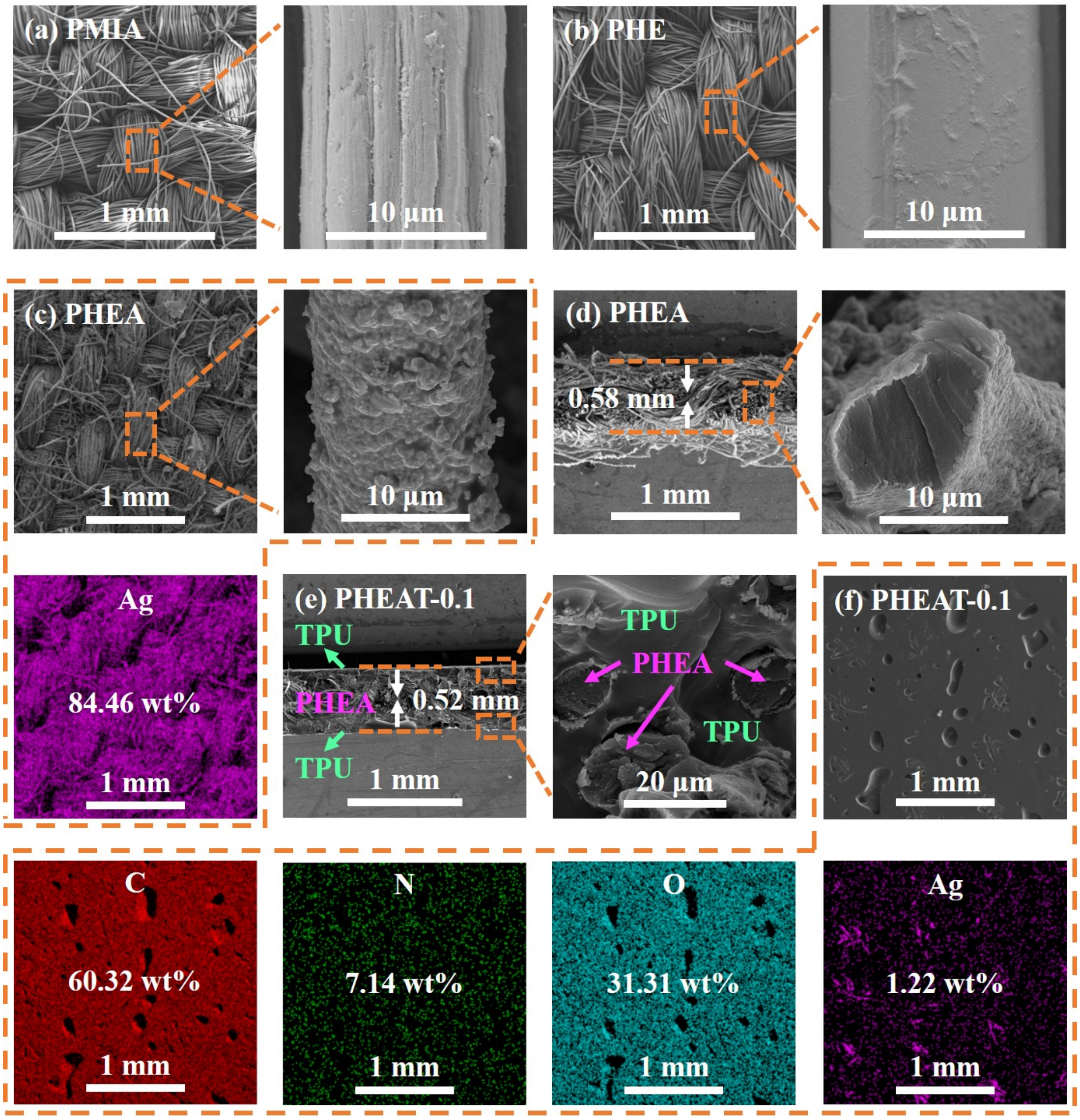

Figure 2. Morphological properties of PHEAT. (**a**–**c**,**f**) Surface SEM images and corresponding elemental mapping of C, N, O, and Ag; (**d**,**e**) Cross-sectional SEM images; (**e**) SEM image showing the thickness of the sandwich-structured TPU-PHEA-TPU and the architecture of brick (PHEA fiber)-mortar (TPU).

3.2. EMI Shielding Performance and Mechanism

High conductivity is essential for effective EMI shielding [27]. PHEAT-0.05 exhibits a low sheet resistance (20.82 m$\Omega \cdot sq^{-1}$) and high conductivity (319 $S \cdot cm^{-1}$), which is comparable to PHEA (422 $S \cdot cm^{-1}$) (Figure 3a). Yet the conductivity drops sharply with the increasing of TPU thickness, inducing a gradual decreasing tendency of SE_T within X-band (Figure 3b). Specifically, the average SE_T decreases from 107.66 dB for PHEA to 101.57 dB for PHEAT-0.05, 73.94 dB for PHEAT-0.1, 59.55 dB for PHEAT-0.15, 43.36 dB for PHEAT-0.2, 49.58 dB for PHEAT-0.25, and 46.14 dB for PHEAT-0.3 with the thickening of TPU from 0, to 0.05, 0.1, 0.15, 0.2, 0.25, and 0.3 mm, in turn. The exposed Ag in the uncovered regions on PHEAT-0.05 maintains an integrated conductive network (Figure S1d), enabling the average EMW attenuation of 99.99999999% across X-band (Figure 3g). The small amount of exposed Ag on PHEAT-0.1 still allows the formation of closed conductive paths (Figure S1e), which achieves the average $SE_{\%}$ of 99.99999583% across the X-band. Although the conductive propagation pathways progressively diminish as the TPU layer thickens (Figure S1f,g), all of the PHEAT samples excel the commercial shielding requirement of 99% (SE_T > 20 dB), with the average $SE_{\%}$ throughout the X-band of 99.99972894% for PHEAT-0.15, 99.99343270% for PHEAT-0.2, 99.99854106% for PHEAT-0.25, and 99.99612211% for PHEAT-0.3, respectively [5]. To further objectively evaluate the superiority of the as-constructed sandwich and brick-mortar architectures, as illustrated in Figure 3c and Table S2, the average SE_T and thickness of PHEAT are compared with those of currently known CPFCs. The comparison confirms that PHEAT-0.05 and PHEAT-0.1, with similarly thin thicknesses of 0.50 and 0.52 mm, respectively, exhibit conspicuous average SE_T

within the X-band, far outperforming other CPFCs [5,22,28–34]. It is noteworthy that the shielding performance (Figure 3d–f) of PHEAT-0.05 and PHEAT-0.1 shows almost no degradation after exposure to various temperature/humidity conditions and rigorous mechanical washing (Figure S3), with only a slight decrease observed after 6 months of storage. This demonstrates the potential environmental stability of PHEAT and suggests that TPU can effectively delay the oxidation and degradation of Ag.

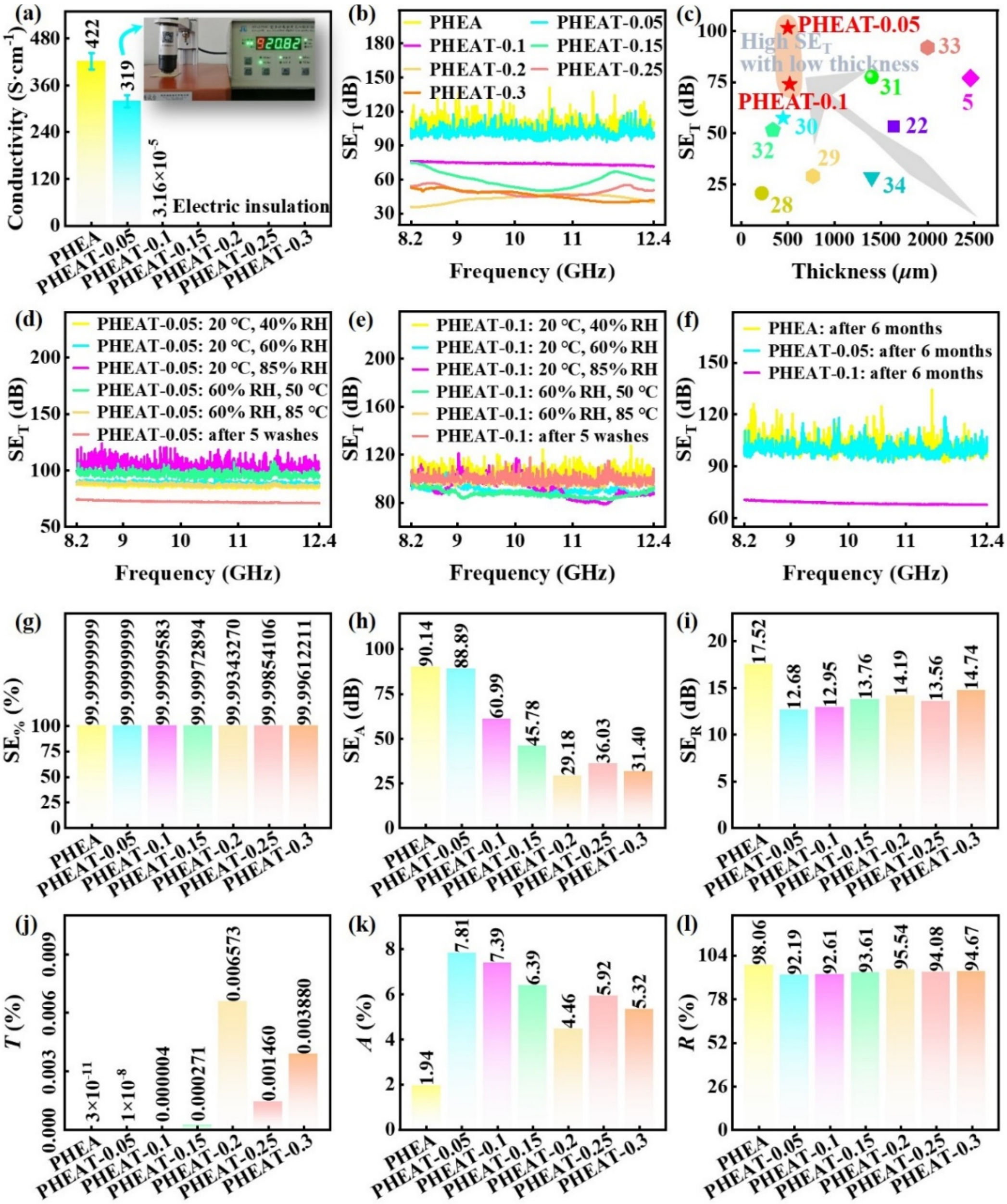

Figure 3. Conductivity and EMI shielding performance of PHEAT. (**a**) Conductivity of PHEAT. Inset shows the four-probe conductivity measurement setup; (**b**) Frequency dependence profiles of SE_T; (**c**) Ashby plot of average SE_T of PHEAT within X-band frequency range versus thickness as compared to those of recently reported CPFCs. The numbers adjacent to the symbols indicate the reference numbers; (**d**–**f**) SE_T of PHEAT after exposure to various relative humidity (RH) and temperature, repeated washing, and storage for 6 months; (**g**–**l**) Histograms of the average value of (**g**) $SE_{\%}$, (**h**) SE_A, (**i**) SE_R, (**j**) *T*, (**k**) *A*, and (**l**) *R* within X-band.

To preliminarily explore the X-band EMW attenuation mechanism of PHEAT, the absorption loss, SE_A, and surface reflection loss, SE_R, are calculated and presented in Figure 3h,i, respectively. As can be seen, the average SE_R always maintains constant around 13 dB across the X-band. Meanwhile, the average SE_A decreases with the increasing TPU thickness, which mirrors the trend of average SE_T, suggesting that the reduction in SE_T is most attributed to the diminished contribution of SE_A. Although the average SE_A exceeds the average SE_R across all samples, it does not necessarily indicate that attenuation is predominantly driven by absorption. This is because

SE_A represents the shielding ability to attenuate EMW that have entered the interior of the CPFCs after being reflected [4]. To gain profounder insight into the EMW attenuation mechanism of PHEAT in terms of energy dissipation, the power coefficients of EMW transmission (T) (Figure 3j), absorption (A) (Figure 3k), and reflection (R) (Figure 3l) are determined using scattering parameters. The T of all samples are low, with the values smaller than 0.0001, underscoring the minimal EMW leakage and further demonstrating their eminent EMI shielding competence [28,35,36]. Most importantly, the R of all PHEAT is markedly higher than their A, indicating that the CPFCs primarily depend on the reflection-dominant shielding mechanism [37]. To accurately validate the actual far-field EMW reflection-dominant dissipation mechanism of PHEAT under realistic conditions, *RCS* simulation was conducted using a CST Studio Suite 2022 software with PEC as a reference. Figure 4b illuminates the modeling setup, Figure 4c–e present the 3D reflection signal intensity distributions of PEC, PHEAT-0.05, and PHEAT-0.1 at 10 GHz within X-band, and Figure 4f–h show the distributions of the corresponding 2D *RCS* values. PEC, a canonical reflective EMI shield, produces strong reflection signals at 10 GHz (Figure 4c), resulting in *RCS* values greater than -20 dB·m^2 across the angular sweeps from −90° to 90° (Figure 4f) [15,23]. As expected, simulations for PHEAT-0.05 (Figure 4d,g) and PHEAT-0.1 (Figure 4e,h) exposed to 10 GHz EMW clearly show that their reflection signal intensities and *RCS* values closely match those of PEC over the entire detection angles from −90° to 90°, thereby conclusively corroborating the reflection-dominated X-band EMW shielding mechanism of PHEAT. Based on the consistency between the simulated and the measured results, it is reasonable to conclude that the PHEAT CPFCs, as an advanced EMW shield, hold significant potentials for electromagnetic pollution preventions, such as chassis lining and aircraft skin shielding layer. Figure 4a visually delineates the attenuation process of an EMW incident on PHEAT, which highlights the multifaceted shielding pathways. When an incident EMW impinges on the material surface, part of it is reflected directly, collectively caused by an impedance mismatch at the interface between exposed Ag particles (high conductivity) and free space (low conductivity), along with abundant mobile charge carriers of Ag [37]. Most EMW entering the material undergoes multiple internal reflections between interlacement-structured Ag-coated fibers and among Ag particles on fiber surfaces. A small portion is absorbed and dissipated as heat during propagation [11]. When absorption exceeds 10 dB, multiple reflections are negligible and included in the absorption loss [38]. Consequently, only a minuscule unattenuated portion transmits through PHEAT, resulting in the observed shielding effect [39].

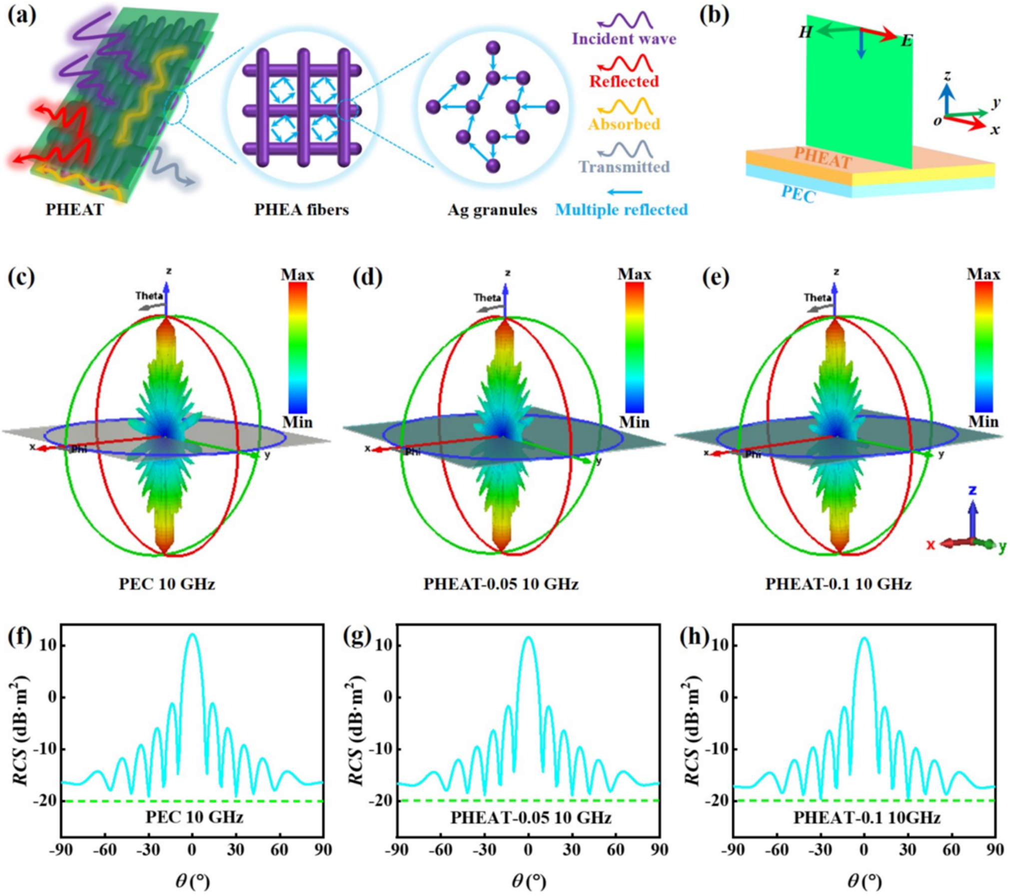

Figure 4. EMI shielding mechanism. (**a**) Schematic diagram showing the EMW loss mechanism; (**b**) Schematic diagram for the *RCS* simulation model; (**c**–**e**) 3D *RCS* maps; (**f**–**h**) 2D *RCS* values as a function of scanning angle.

3.3. Abrasion Resistance Performance

Robust abrasion resistance is critical for sustained EMI shielding. Hence, the abrasion durability of Ag, PDMS, and TPU coatings were evaluated for the EMI shielding efficiency of the corresponding CPFCs (Table S3) using a fastness tester as depicted in Figures 5a and S4a. For a typical test, the sample was abraded back-and-forth over a 104 mm distance at 120 cycles·min^{-1} using 600-, 1000-, or 1500-grit sandpaper affixed to a 16-mm-diameter abrasion head designed to exert a 9 N load (equivalent to ≈45 kPa pressure) [19]. Following the abrasion, the surface topology, elemental distribution and content of Ag, as well as SE_T of the sample were analyzed to determine the robust durability and effectiveness of the hot-pressed TPU layer. Moreover, to enhance the clarity of the abrasion results and make them more intuitive for readers, the optical images of all specimens are provided in Figure S4. As can be seen, PHEA suffers severe Ag layer peeling after only 100 cycles of abrasion with 1500-grit sandpaper (Figures S4b,f and S5a), and the average SE_T drops to 34.12 dB in the frequency range of X-band (Figure 5b). Similarly, PHEAP (average SE_T = 103.79 dB) undergoes severe PDMS and Ag layer destructions in the first 100 abrasion cycles with 600-, 1000-, or 1500-grit sandpaper (Figures S4c,g and S5c), which reduces the average SE_T to 32.84, 37.41, and 46.37 dB across the frequency range of X-band, respectively (Figure 5c), with the minimum retention of 31.64%, unambiguously demonstrating inadequate protection. In stark contrast, PHEAT samples were able to endure 1000 abrasion cycles. Despite its ultrathin 0.05 mm TPU layer, PHEAT-0.05 maintains the average SE_T values above 48.18% after abrasion, 52.95 dB (600-grit), 52.22 dB (1000-grit), and 48.94 dB (1500-grit), across the X-band (Figure 5d). Visible abrasion marks (Figure S4d,h) and exposed fibers/Ag (Figure 5g,h) are observed, and the average SE_T slightly increases as the rougher sandpapers are used (Figure 5d). This trend aligns well with the Ag content (Figure 5g–i), suggesting that the conductive network remains essentially functional. PHEAT-0.1 shows prominent retention of the shielding effectiveness after abrasion (>80.65%) with the average SE_T = 59.63 dB (600-grit), 65.37 dB (1000-grit), and 71.19 dB (1500-grit) across X-band (Figure 5e). This performance is attributed to the minimal surface damage (Figures 5j–l and S4e,i), which preserves the conductive pathways. These results indicate that, despite being subjected to intense abrasion, PHEA-0.05 and PHEAT-0.1 can still maintain noticeable SE_T due to their structural stability, which is essential for their performance in real-world applications. The thicker TPU layers on PHEAT-0.15 and PHEAT-0.2 offer near-complete physical barriers under 600-grit abrasion for 1000 cycles (Figure 5m,n), retaining 89.20% (53.12 dB) and 91.84% (39.82 dB) of their initial SE_T, respectively (Figure 5f). This demonstrates their robust mechanical abrasion resistance and significantly extended operational lifespan. In summary, the remarkable abrasion robustness and higher SE_T retention enabled by the ingeniously devised sandwiched and brick-mortar structures highlight the advantage of PHEAT for long-term operation in complex application scenarios over PHEAP.

3.4. Strain Sensing Performance

The high conductivity and excellent flexibility, along with the ultra-robust sandwiched and brick-mortar structures of PHEAT-0.05 make it a promising candidate of extraordinary strain sensor. Bending PHEAT by applying an external force densifies the contact area between conductive fibers, thereby enriching the conductive network, and increasing the overall conductivity of the sensor (Figure 6a,b). Herein, the strain sensing performance of PHEAT-0.05 was evaluated by monitoring its relative resistance change, $(R - R_0)/R_0$ (R and R_0 represent the real-time resistance at strain and initial resistance before bending), during cyclic bending. Strain parameters including position 1 (30 mm), position 2 (20 mm (33% strain), 15 mm (50%), 10 mm (67%), or 5 mm (83%)), 0 s delay at positions, and motion rates of 50, 100, or 200 mm·s^{-1} were used. PHEAT-0.05 demonstrates excellent sensing repeatability under varying bending strain rates (50, 100, 200 mm·s^{-1}, Figure 6b–d) and strain amplitudes (33%, 50%, 67%, 83%, Figure 6c,e–g), which is attributed to the stress-protective role of TPU. Figure S6a–c and Table S4 compare the sensing performance of PHEAT-0.05 with other CPFCs strain sensors. The response and recovery times of PHEAT-0.05 are only 160 ms and 180 ms, respectively, and its speed surpasses that of most CPFCs strain sensors. More importantly, PHEAT-0.05 reveals stable response signal to bend strain throughout 1000 cycles bending-releasing, highlighting the excellent durability and long-term reliability of the sensor (Figure S6d–g). In addition, the compatibility of TPU with human body further enhances its practicality in movement monitoring, enabling PHEAT to be attached to various body parts and track motions using resistance signals. As presented in Figure 6h, PHEAT-0.05 positioned on the index finger can identify bending motion in real-time. During finger bending and releasing cycles, PHEAT-0.05 demonstrates reliable resistance signals (Figure 6i). Similarly, it can steadily detect the bending motions of wrist, elbow and knee (Figure 6j–l), confirming its responsiveness to joint movements [37,40]. In conclusion, owing to their superior performance and dual functionality, the PHEAT CPFCs show strong application potentials in next-generation smart flexible electronic devices, aiding bright prospect for EMI shielding and human motion sensing.

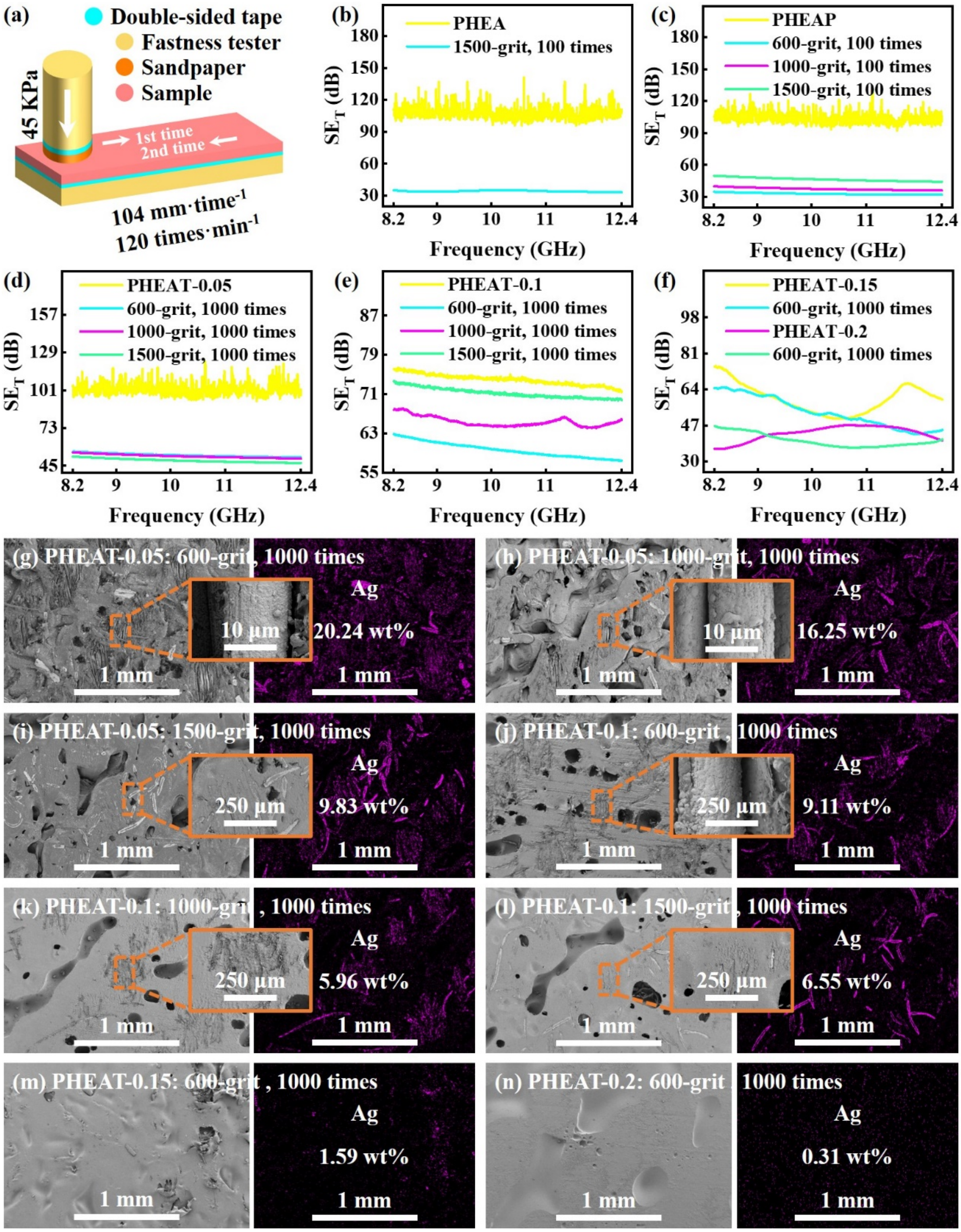

Figure 5. Abrasion resistance functionality. (**a**) Schematic diagram of the setup for sandpaper abrasion test; (**b**–**f**) SE_T frequency response curves after abrasion; (**g**–**n**) SEM and corresponding Ag elemental mapping images after abrasion.

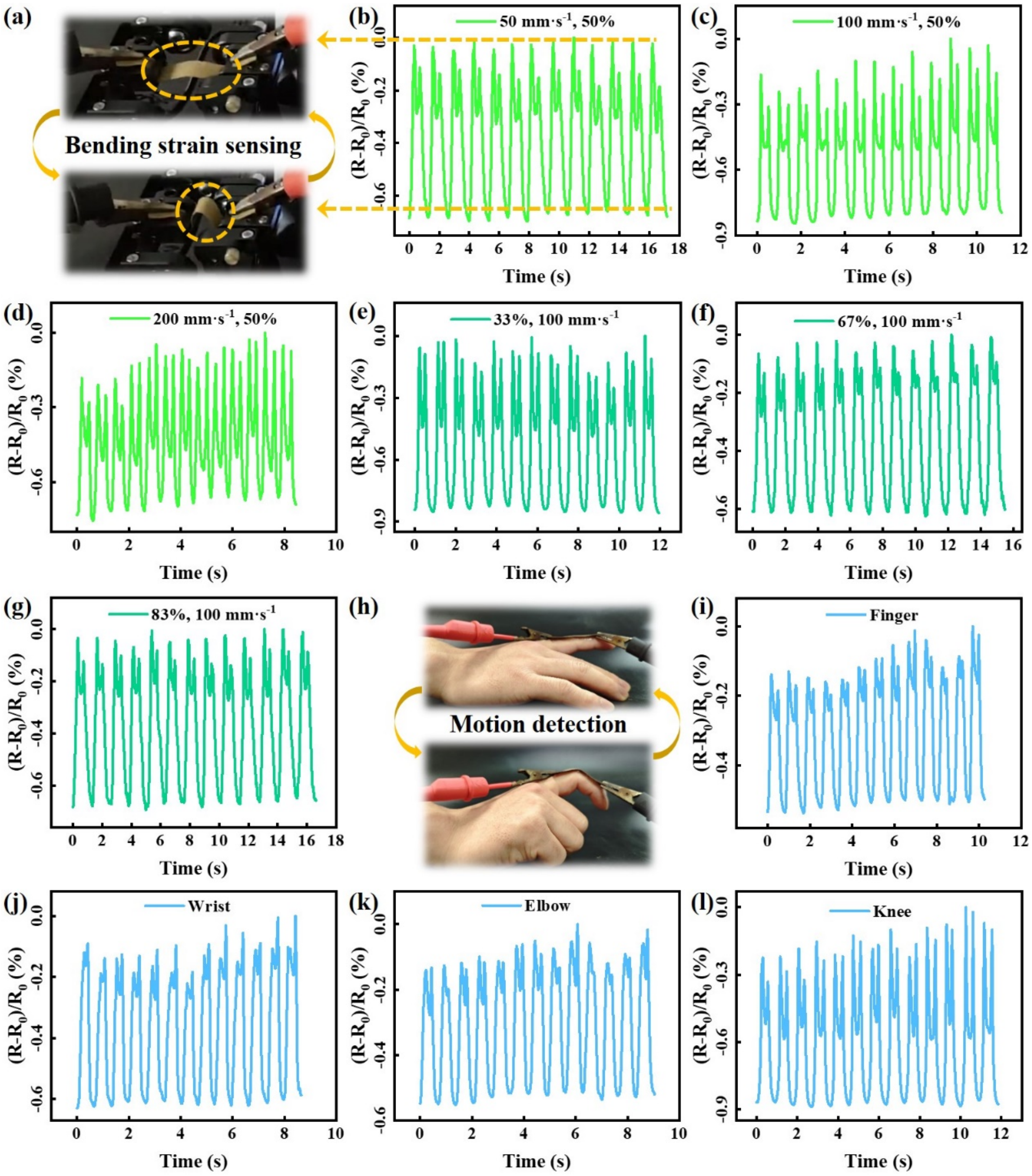

Figure 6. Strain sensing performance of PHEAT-0.05. (**a**) Device for bending strain sensing test; (**b**–**g**) Relative resistance change responses under varying strain rates (**b**–**d**) and amplitudes (**e**–**g**); (**h**) Application of PHEAT-0.05 sensor to finger joint for real-time motion monitoring; (**i**–**l**) Relative resistance change response to the bending motions of (**i**) finger (**j**) wrist (**k**) elbow and (**l**) knee.

4. Conclusions

An ultra-robust EMI shielding and strain sensing composite, PHEAT, has been successfully engineered by integrating HPAMAM-EGDE surface activation, electroless Ag plating, and hot-pressing with TPU and characterized. The HPAMAM-EGDE modifier, rich in amino/carbonyl groups and nanoscale cavities, can facilitate efficient Ag deposition and enhance the interfacial adhesion to PMIA substrate. The hot-pressing process creates an internal brick (PHEA fiber)-mortar (TPU) microstructure and an external TPU-PHEA-TPU sandwich macrostructure. This unique geometric architecture considerably augments the mechanical strength of the Ag-plated fabric (PHEA), while preserving the inherent pliability, lightweight, and thinness of PMIA fabric. Importantly, PHEAT exhibits conspicuous abrasion resistance. PHEAT-0.05 (SE_T = 101.57 dB) and PHEAT-0.1 (SE_T = 73.94 dB) incorporating just 0.05- and 0.1-mm-thick of TPU, respectively, still offer the SE_T values of 52.95 dB and 59.63 dB after 1000 cycles of vigorous abrasion using 600-grit sandpaper, corresponding to the EMW shielding efficiency of 99.99949% and 99.99989%. Whereas, the SE_T of PHEA (107.66 dB) and PHEAP (103.79 dB) decreased to 34.12 dB and 46.37 dB, respectively, after only 100 abrasion cycles with 1500-grit sandpaper, which highlights the superior protective role of TPU compared to PDMS for PHEA in harsh physical conditions. Furthermore, the composite shows reliable and repeatable relative resistance change under cyclic bending strain and human joint movements due to the reversible densification of the internal conductive fiber network, showcasing its immense potential for flexible sensing applications. The balance between effective EMI shielding, sensing proficiency and exceptional abrasion-resistant performance can be accounted for by two key factors:

(i) At the material level, Ag and TPU offer excellent conductivity, flexibility and robustness; (ii) At the structural level, the tightly-riveted brick-mortar and sandwich architectures impart remarkable fatigue resistance and reliability, making PHEAT a strong candidate for next-generation flexible electronic devices. Collectively, this study presents a new paradigm for developing multifunctional, ultra-abrasion-resistant composites and offers valuable insights into the design of high-performance polymer fabric-based materials.

Supplementary Materials

The additional data and information can be downloaded at: https://media.sciltp.com/articles/others/2603121102178846/EWST-25120179-SI.pdf. Figure S1: Microstructure of PMIA, PHE, PHEA and PHEAT. (**a–g**) SEM and corresponding C, N, O, Ag elemental mapping images; (**h–l**) SEM images demonstrating thickness. Figure S2: Microstructure of PHEA and PHEAT-0.1. Cross-sectional SEM and corresponding C, N, O, Ag elemental mapping images (**a**) PHEA (**b**) PHEAT-0.1. Figure S3: Environmental stability. Digital photos of (**a,c**) PHEAT-0.05 (**b,d**) PHEAT-0.1 before and after exposure to various temperature (°C) and relative humidity (RH), and 5 washing cycles. Figure S4: Abrasion resistance test. (**a**) A digital picture of the measurement setup; (**b–e**) Optical images of PHEA, PHEAP, PHEAT-0.05, and PHEAT-0.1 before and after sandpaper abrasion; (**f–i**) Mass loss of PHEA, PHEAP, PHEAT-0.05, and PHEAT-0.1 after abrasion. Figure S5: Microstructure of PHEA and PHEAP. SEM photographs and elemental mappings of (**a**) PHEA after abrasion test, PHEAP before (**b**) and after (**c**) abrasion test. Figure S6: Sensing performance of PHEAT-0.05. (**a–c**) Response speed of the PHEAT-0.05; (**d–f**) Durability of PHEAT-0.05 over 1000 cycles. Table S1: Summary of sample codes and abbreviations. Table S2: A comprehensive comparison of SE_T, density, and the thickness of state-of-the-art CPFCs. Table S3: A comprehensive comparison of abrasion resistance performance. Table S4: A comparison of sensing performance with representative CPFCs strain sensors reported in recent literature. References [41–49] are cited in the supplementary materials.

Author Contributions

J.W.: data curation, formal analysis, investigation, software, writing-original draft preparation; R.Q.: conceptualization, funding acquisition, project administration; X.L., J.L. and L.G.: validation, visualization; F.M., Y.Z., Y.W. and C.S.: supervision, writing-reviewing and editing; X.S., Q.M., X.G., X.K. and R.A.: methodology, resources. All authors have read and agreed to the published version of the manuscript.

Funding

This research was funded by the Yantai City Major Science and Technology Innovation Project (2024ZDCX016), the Natural Science Foundation of Shandong Province (ZR2025MS725), and the National Natural Science Foundation of China (52073135). The article processing charges was funded by Yantai City Major Science and Technology Innovation Project (2024ZDCX016).

Data Availability Statement

The data that support the findings of this study are available from the corresponding author upon reasonable request.

Conflicts of Interest

The authors declare no conflict of interest.

Use of AI and AI-Assisted Technologies

No AI tools were utilized for this paper.

References

1. Zhang, J.; Xu, T.; Ding, L.; et al. Bridging graphene for films with superior mechanical and electrical performance for EMI shielding. *eScience* **2025**, *5*, 100407.

2. Malekie, S.; Madani, S.S.; Molhem, H.; et al. Analysis of the EMI shielding effectiveness of polystyrene-SWCNT nanocomposite in X-band frequencies. *J. Nanopart. Res.* **2025**, *27*, 42–54.
3. Guo, M.; Guo, X.; Niu, H.; et al. Entire X broadband and high-performance electromagnetic wave absorbing Ni/liquid metal/graphene oxide/bacterial cellulose composite films. *J. Mater. Sci. Mater. Electron.* **2025**, *36*, 159–172.
4. He, L.; Shao, X.; Tian, M.; et al. Superhydrophobic and durable Ag-coated fabrics for efficient EMI shielding. *ACS Appl. Eng. Mater.* **2023**, *1*, 851–860.
5. Tang, X.; Lu, Y.; Li, S.; et al. Hierarchical polyimide nonwoven fabric with ultralow-reflectivity EMI shielding and high-temperature resistant infrared stealth performance. *Nano-Micro Lett.* **2024**, *17*, 82–100.
6. Zhou, Y.; Li, W.; Li, L.; et al. Lightweight and highly conductive Ag nanoparticles functionalized PMIA nonwoven fabric for enhanced EMI shielding. *J. Mater. Sci.* **2021**, *56*, 6499–6513.
7. Rajan, A.; Solaman, S.K.; Ganesanpotti, S. Electromagnetic simulation integrated strategy to metamorphose commercial cotton into multifunctional EMI shielding fabrics. *Adv. Compos. Hybrid Mater.* **2025**, *8*, 203–230.
8. Jiang, B.; Li, N.; Wang, Y.; et al. Ultralight and flexible electrospun PMIA/AgNW/Ni composite membrane with thermostability and excellent EMI shielding effectiveness. *J. Alloys Compd.* **2023**, *960*, 170993.
9. Wang, H.; Yao, L.; Lu, H.; et al. Construction of concave microstructures inspired by papilio ulysses telegonus wing onto Ag-printed fabrics with low-cost, flexible, and lightweight for superior EMI shielding. *Colloid Surf. A Physicochem. Eng. Asp.* **2025**, *716*, 136646.
10. Wang, Q.; Wang, Y.; Sun, C.; et al. Multifunctional aramid nanofiber/MXene/aramid fiber composite fabric with outstanding EMI shielding performance. *Coatings* **2025**, *15*, 354–366.
11. Zhang, T.; Guo, J.; Liu, S.; et al. Enhanced electroless metallization of aramid fibers via non-destructive π–π surface engineering for EMI shielding. *Compos. Sci. Technol.* **2025**, *269*, 111236.
12. Li, X.; Zhou, S.; Ji, Z.; et al. Fabrication of conductive polyimide/metal composite fibers for high temperature EMI shielding. *Appl. Surf. Sci.* **2025**, *680*, 161293.
13. Manogaran, R.; Murugesan, M. A review on recent advancements in textile fabrics for EMI shielding materials. *Mater. Today Commun.* **2025**, *44*, 111879.
14. Li, L.; Sun, B.; Li, W.; et al. Flexible and highly conductive AgNWs/PEDOT:PSS functionalized aramid nonwoven fabric for high-performance EMI shielding and joule heating. *Macromol. Mater. Eng.* **2021**, *306*, 2100365.
15. Wang, J.; Qu, R.; Ren, B.; et al. Lightweight, flexible, resilient PMIA-based fabric with superior EMI shielding performance. *Adv. Fiber Mater.* **2025**, *7*, 784–798.
16. Su, X.; Lai, S.; Yang, S.; et al. Graphene stripping, a convenient and environmentally friendly technology for the preparation of polyurethane/graphene nanocomposites as a new type of highly wear-resistant materials. *J. Appl. Polym. Sci.* **2023**, *140*, e54617.
17. Dai, K.; Xie, H.; Wei, Q.; et al. Polyurethane Ni lacquer coated carbon fiber cloth with excellent mechanical properties and high EMI shielding performance. *Prog. Org. Coat.* **2025**, *198*, 108905.
18. Cao, W.; Wu, L.; Zhai, Y.; et al. Tough, highly transparent, and wear resistant polyurethane-calcium phosphite oligomer organic-inorganic hybrid nanocomposite. *ACS Appl. Polym. Mater.* **2024**, *6*, 5080–5088.
19. Wen, X.; Li, H.; Li, R.; et al. Coral-inspired superhydrophobic triboelectric nanogenerators with unprecedented wear resistance and sub-zero temperature self-healing capability. *Adv. Funct. Mater.* **2025**, *35*, 2501706.
20. Feng, M.; Feng, S.; Yu, T.; et al. Versatile and comfortable janus fabrics for switchable personal thermal management and EMI shielding. *Adv. Fiber Mater.* **2024**, *6*, 911–924.
21. Zhao, X.; Li, L.; Li, Y.; et al. Biobased thermoset sandwiched composites enabled by dynamic covalent chemistry for electrical insulation, EMI shielding, and thermal management. *SusMat* **2025**, *5*, e70012.
22. Zhu, Y.; Chen, M.; Yan, J.; et al. MXene/CuNWs composite fabric with biomimetic leaf-like hierarchical structure for EMI shielding, dual-driven heating, infrared stealth and self-cleaning. *Compos. Pt. A Appl. Sci. Manuf.* **2025**, *193*, 108860.
23. Wu, S.; Wang, C.; Tang, Y.; et al. Metal-organic framework-derived hierarchical Cu_9S_5/C nanocomposite fibers for enhanced electromagnetic wave absorption. *Adv. Fiber Mater.* **2024**, *6*, 430–443.
24. Wang, J.; Qu, R.; Wang, Q.; et al. Interface construction of crosslinked HPAMAM between Ag layer and PMIA fiber to enhance conductivity and its resilience to adverse conditions. *Surf. Interfaces* **2024**, *53*, 104983.
25. Tao, W.; Shao, W.; Ma, M.; et al. Ag anchored mesoporous carbon hollow sphere in cellulose nanofibers/MXene composite films for high-performance EMI shielding. *Nano Mater. Sci.* **2025**, *7*, 65–73.
26. Cheng, M.; Xu, X.; Zhang, H.; et al. Self-assembling, flexible and stable aramid nanofiber/polypyrrole/MXene composite film for efficient EMI shielding, dual-driven heating and infrared thermal camouflage. *Chem. Eng. J.* **2025**, *505*, 159112.
27. Jin, Y.H.; Han, J.H.; Park, J.; et al. Water- and oxidation-resistant MXenes for advanced EMI shielding applications. *InfoMat* **2025**, *7*, e70034.
28. Li, X.; Zhang, C.; Gong, S.; et al. Biobased protective nonwovens integrating thermal management, antifouling, and absorption-dominated EMI shielding via melt centrifugal spinning. *Macromolecules* **2025**, *58*, 2649–2660.

29. Xie, J.; Shi, L.; Wang, J.; et al. Polarizaton-layered core-sheath architectured $Ti_3C_2T_x$@ZnO@carbon fabric composites for broadband high-absorption EMI shielding. *Adv. Funct. Mater.* **2025**, *35*, e09048.
30. Tang, X.; Gao, H.; Zhao, X.; et al. Gradient-structured polyimide nonwoven fabrics for intelligent adjustable low-reflection EMI shielding. *Mater. Today Nano* **2025**, *29*, 100586.
31. Lu, J.; Yu, Y.; Zhang, Y.; et al. Flexible protective cotton fabrics based on multi-layer nano coating: Sustaining EMI shielding capabilities in fire conditions. *Prog. Org. Coat.* **2025**, *201*, 109131.
32. Liao, P.; Wang, C.; Huang, W.; et al. Optimizing EMI shielding of flexible textiles using SiC@C nanowhiskers synthesized via laser chemical vapor deposition. *Appl. Surf. Sci.* **2025**, *689*, 162436.
33. Han, W.; Huang, K.; Yu, Q.; et al. Electrostatic interaction-inspired textiles based on MXene decoration for superior EMI shielding, infrared thermal camouflage, and fire proofing. *Colloid Surf. A Physicochem. Eng. Asp.* **2025**, *718*, 136934.
34. Singh, K.; Baheti, V. EMI shielding and joule heating applications of woven and nonwoven activated carbon fabrics of kevlar fibres. *J. Anal. Appl. Pyrolysis* **2025**, *188*, 107041.
35. Wei, M.; Wu, N.; Li, B.; et al. From MXene to multimodal-responsive smart, durable EMI shielding textiles. *Adv. Funct. Mater.* **2025**, *35*, 2424312.
36. Song, M.; Liu, Z.; Wang, Y.; et al. Industrial-grade flexible carbon fiber paper/MXene composite EMI shielding material with ultra-large area and ultra-high performance. *Adv. Funct. Mater.* **2025**, *35*, 2421422.
37. Suryaprabha, T.; Hong, S.; Pham, T.; et al. Superhydrophobic, self-cleaning MWCNT/Ferrite/Ni chain/PDMS-coated cotton fabrics for wearable applications: EMI shielding and underwater alerts. *Chem. Eng. J.* **2025**, *507*, 160378.
38. Li, Y.; Wang, Y.; Li, Z.; et al. Meter-scale wearable multifunctional core-shell nanofiber textiles for ultra-broadband EMI shielding and infrared stealth. *Adv. Mater.* **2025**, *37*, 2501485.
39. Jiang, B.; Shang, J.; Zhang, F.; et al. Multifunctional, efficient, and durable composites of conductive PMIA/Ag membrane. *Compos. Pt. A Appl. Sci. Manuf.* **2024**, *185*, 108372.
40. Zong, P.; Chen, M.; Wang, X.; et al. Coating carbon cloth with Cu_3Se_2 by electrodeposition for pressure sensing and enhanced EMI shielding. *Carbon* **2025**, *232*, 119814.
41. Zhao, X.; Zhang, P.; Zhang, S.; et al. Breathable, robust, and flexible hierarchical design of multifunctional integrated smart textiles for human health management. *Chem. Eng. J.* **2025**, *507*, 160736.
42. Xiao, W.; Wu, H.; Su, Q.; et al. MXene initiated in situ construction of superhydrophobic and electrically conductive nanofibrous composites for wearable multifunctional sensing. *Chem. Eng. J.* **2025**, *508*, 161074.
43. Fan, B.; Tian, X.; Dong, S.; et al. Fabric/hydrogel sandwich-structured flexible sensor with broad sensing range for pressure and temperature sensing. *Chem. Eng. J.* **2025**, *526*, 171363.
44. Pan, S.; Wang, W.; Lin, C.; et al. High-performance $Ti_3C_2T_x$ MXene-based fabric pressure sensor with TA-assisted antioxidant stability for human monitoring and scalable sensing array application. *Sensor. Actuat. A Phys.* **2026**, *397*, 117247.
45. Du, X.; Song, Y.; Du, C.; et al. Multifunctional microfluidic-directed polymer/hydrogel fabrics towards pH-responsive drug delivery, wound monitoring and wearable sensing. *J. Control. Release* **2026**, *390*, 114565.
46. Cui, Y.; Chen, Q.; Bao, W.; et al. Dual-catalytic polymerization of high-performance PEDOT thermoelectric fabrics for self-powered sensing. *Chem. Eng. J.* **2025**, *523*, 168819.
47. Srinivasan, R.; Ravi, S.A. A long-term stable flexible pressure sensor based on MWCNT/PEDOT:PSS-coated crepe bandage for wide-range sensing. *Mater. Lett.* **2026**, *406*, 139894.
48. Chen, Q.; Jiang, H.; Lv, Z.; et al. Scalable fabrication of stretchable hierarchical spiral-wrapped yarns for strain-insensitive pressure sensing. *Appl. Mater. Today* **2026**, *48*, 103088.
49. Gu, W.; Liu, J.; Su, X.; et al. Construction of protective layer on PET fabric by utilizing hydrophilic-hydrophobic interactions for sensing, flame retardancy and thermal management properties. *Chem. Eng. J.* **2025**, *520*, 165744.